Modulational instability and critical regime in a highly birefringent fiber

E. Seve, P. Tchofo Dinda, G. Millot, and M. Remoissenet
Laboratoire de Physique de l'Université de Bourgogne, URA 1796 CNRS, BP 138, 21004 Dijon, France

J. M. Bilbault
Laboratoire LIESIB de l'Université de Bourgogne, 6 Boulevard Gabriel, 21100 Dijon, France

M. Haelterman
Université Libre de Bruxelles, Service d'Optique, CP 194/5, 50 av. Roosevelt, B-1050 Bruxelles, Belgium
(Received 3 May 1996)

We report experimental observations of modulational instability of copropagating waves in a highly birefringent fiber for the normal dispersion regime. We first investigate carefully the system behavior by means of nonlinear Schrödinger equations and phase-matching conditions, and then, experimentally, we use two distinct techniques for observing MI (modulational instability) in the fiber; namely, the single-frequency copropagation, where two pump waves of identical frequency copropagate with orthogonal polarizations parallel to the two birefringence axes of the fiber, and the two-frequency copropagation, where the two polarized waves copropagate with different frequencies. In both cases the GVM (group-velocity mismatch) of the two copropagating waves appears as the particularly important parameter which governs the system behavior. For the single-frequency copropagation, the GVM is simply proportional to the intrinsic birefringence of the fiber and therefore varies only very slightly versus the wavelength, and there exists a nonzero critical power for the input wave above which MI vanishes [Phys. Rev. A **42**, 682 (1990)]. In the two-frequency-copropagation regime, however, the GVM becomes a variable parameter, that is, a real *control parameter* for MI, whose value can be easily tuned over a wide range by just changing the wavelength separation between the two pump waves. For several values of the GVM we show that the two-frequency-copropagation regime provides a richer spectrum of behavior than the single-frequency copropagation. Most of the richness comes from the existence of particular values of pump wavelengths for which MI disappears for all input-wave power, that is, the existence of a *critical regime* in which the critical power becomes zero. This behavior is drastically different from what was previously observed in the single-frequency configuration. [S1050-2947(96)02710-2]

PACS number(s): 42.65.Re, 42.81.Dp

I. INTRODUCTION

Several remarkable nonlinear phenomena have already been observed in optical fibers. A typical example is the MI (modulational instability) phenomenon, which is an effect induced by the interaction between nonlinear and dispersive effects [1]. More specifically, MI is a phenomenon in which a continuous wave propagating in a nonlinear medium undergoes, in the presence of weak noise or any other small perturbation, a modulation of its amplitude or phase, which can ultimately end up in breaking up the wave into small pulses (solitons).

Although the instability of electromagnetic waves propagating in nonlinear media was already predicted many decades ago [2–4], the first experimental observation of MI in an optical fiber was obtained only in the last decade [5]. The experimental evidence was then given that MI can be observed in a nonbirefringent fiber with anomalous group-velocity dispersion [5]. This result has been confirmed subsequently by other observations of MI in the anomalous dispersion regime [6–10].

There has also been a considerable effort to gain insight into MI processes in birefringent fibers [11–19]. One of the main results of these studies was obtained by Wabnitz [15], who carried out a theoretical analysis of the single-frequency-copropagation regime and demonstrated that MI can occur for the normal dispersion regime in a weakly birefringent fiber. The experimental evidence was given subsequently by Rothenberg [20] and Drummond and co-workers [21], who observed MI of optical waves copropagating in the normal dispersion regime in strongly birefringent fibers, and recently by Murdoch and co-workers [22], who observed MI in weakly birefringent fibers. The technique used in those experiments [20–22] for obtaining MI is the single-frequency copropagation. An interesting result in Ref. [20] is the demonstration that there exists a nonzero critical wave power above which MI vanishes; this implies that MI will always occur in the single-frequency-copropagation regime if the input-wave power is sufficiently small.

On the other hand, Drummond and co-workers [21] have pointed out the important feature that the appearance of MI in a highly birefringent fiber is due to the group-velocity mismatch (GVM) between the two copropagating waves. Then, using the classical coupled set of incoherently coupled NLSE (nonlinear Schrödinger equations), they showed that the importance of the MI phenomenon progressively decreases as the GVM decreases, and vanishes when the GVM becomes zero. But Drummond and co-workers [21] left unexplained how one can practically obtain a zero GVM for a single frequency-copropagation regime in a highly birefringent fiber. In fact, in this regime, the GVM is simply propor-

tional to the value of the intrinsic birefringence [20], and therefore a zero GVM corresponds to the limit case where the intrinsic birefringence becomes exactly zero. Consequently, the zero-GVM case considered in Ref. [21], where MI disappears, corresponds in fact to the limit case where the fiber becomes nonbirefringent, which invalidates the coupled NLSE model used to obtain this result.

Parallel to these studies for the single-frequency-copropagation regime for birefringent fibers, there have also been numerous investigations of MI for the two-frequency-copropagation regime, carried out via various theoretical approaches and sometimes supported by numerical simulations [13,23]. One of the main results that emerges from these investigations is the prediction that MI can occur in a highly birefringent fiber for two copropagating frequencies in the normal dispersion regime. Nevertheless, to our knowledge, so far no experimental observation of MI for two copropagating frequencies has been reported to support this prediction.

In the present work, we carefully examine the behavior of a highly birefringent fiber in the normal dispersion regime and provide a general picture describing the outstanding manifestations of the MI process and some related phenomena for single-frequency copropagation as well as for the two-frequency copropagation. In particular we provide experimental observations of MI for two copropagating frequencies in a highly birefringent fiber. We consider several wavelength separations between the copropagating waves, and obtain a richer spectrum of behavior than the behavior found for the typical single-frequency-copropagation regime. We show in particular that there exist critical wavelength separations between the pump waves for which MI never appears, whatever the input-wave power and the fiber length. We refer to this behavior as the ''critical regime.'' Furthermore, as another phenomenon related to MI, we obtain experimental spectra showing Raman effects induced by the sidebands of the pump waves for the single-frequency copropagation as well as for the two-frequency copropagation.

The paper is organized as follows. In Sec. II we briefly review the theoretical description of our system in terms of coupled NLSE and obtain formulas that give the functional dependence of the frequency spectrum upon the GVM, the intrinsic birefringence, and the frequency separation between the pump waves. In Sec. III we present our experimental observations of MI and related phenomena. Finally in Sec. IV we give some concluding remarks.

II. THEORETICAL STUDY

A. Coupled nonlinear Schrödinger equations

The NLSE have been shown to provide an approximate but fairly accurate description of two copropagating waves in birefringent fibers [13,20–23]. In the present work we consider a lossless fiber with a strong intrinsic birefringence, in which two waves, polarized, respectively, along the two birefringence axes, copropagate along the z axis, in the normal dispersion regime. In this subsection we focus on the description of the two-frequency copropagation, where the two waves vibrate at different angular frequencies ω_p and ω_q. Whenever it will be convenient, the single-frequency copropagation can be obtained by just making $\omega_p=\omega_q$. Throughout the paper, the x axis designates the birefringence axis with the lowest refractive index, whereas the y axis designates the birefringence axis with the highest refractive index. Later on, the x and y axes will be simply referred to as the ''fast axis'' and ''slow axis,'' respectively. We will also assume, unless specified, that the wave ω_p is polarized along the fast axis, and ω_q along the slow axis. In this context, each of the frequencies ω_r $(r=p,q)$ is related to a group velocity

$$v_{gx,\omega_p}\equiv\left(\frac{d\omega}{dk_x}\right)_{\omega=\omega_p} \quad \text{and} \quad v_{gy,\omega_q}\equiv\left(\frac{d\omega}{dk_y}\right)_{\omega=\omega_q}, \tag{1}$$

where k_l $(l=x,y)$ designates the wave number components. The corresponding group-velocity-dispersion coefficients are defined by

$$\beta_{2p}\equiv\left(\frac{d^2\omega}{dk_x^2}\right)^{-1}_{\omega=\omega_p} \quad \text{and} \quad \beta_{2q}\equiv\left(\frac{d^2\omega}{dk_y^2}\right)^{-1}_{\omega=\omega_q}. \tag{2}$$

The field amplitude A_r $(r=p,q)$ is related to the input-wave powers[5]

$$P\equiv|A_p|^2, \quad Q\equiv|A_q|^2. \tag{3}$$

Then, expanding k_l $(l=x,y)$ in a Taylor series around the two input-wave frequencies, the amplitudes A_p and A_q of the electric fields are found to satisfy the following set of coupled NLSE:

$$\frac{\partial A_p}{\partial z}+\frac{1}{v_{gx,\omega_p}}\frac{\partial A_p}{\partial t}+\frac{1}{2}\,i\beta_{2p}\frac{\partial^2 A_p}{\partial t^2} =i\gamma_p\left[\left(|A_p|^2+\frac{2}{3}|A_q|^2\right)A_p +\frac{1}{3}A_p^*A_q^2\exp[2i(z\Delta k-t\Delta\omega)]\right], \tag{4}$$

$$\frac{\partial A_q}{\partial z}+\frac{1}{v_{gy,\omega_q}}\frac{\partial A_q}{\partial t}+\frac{1}{2}\,i\beta_{2q}\frac{\partial^2 A_q}{\partial t^2} =i\gamma_q\left[\left(|A_q|^2+\frac{2}{3}|A_p|^2\right)A_q +\frac{1}{3}A_q^*A_p^2\exp[2i(t\Delta\omega-z\Delta k)]\right], \tag{5}$$

where t is the time, $\Delta\omega\equiv\omega_q-\omega_p$, and $\Delta k\equiv k_y-k_x$. In these equations, the nonlinear coefficients are written

$$\gamma_p\equiv\frac{n_2\omega_p}{c(A_{\text{eff}})_p}, \quad \gamma_q\equiv\frac{n_2\omega_q}{c(A_{\text{eff}})_q}, \tag{6}$$

where c designates the light velocity, $n_2=3.2\times10^{-16}$ cm^2/W is the nonlinear index coefficient, and $(A_{\text{eff}})_r$ $(r=p,q)$ designates the effective core area for the wave ω_r. The group-velocity mismatch of the two waves is then defined as

$$\delta \equiv \frac{1}{v_{gy,\omega_q}} - \frac{1}{v_{gx,\omega_p}}. \tag{7}$$

Furthermore, as the variation of the intrinsic birefringence as a function of the frequency is known to be negligible in the parameter regions that are usually considered in practice, the GVM, Eq. (7), can be approximated, for the single-frequency copropagation, by

$$\delta_0 \equiv \frac{B}{c}, \tag{8}$$

where $B \equiv n_y - n_x$ designates the intrinsic birefringence of the fiber. For the two-frequency copropagation, however, the GVM depends not only on the birefringence B, but also on the frequencies of the two pump waves. So, when the frequency interval between the two pump waves is not too large, the GVM is found to be approximately

$$\delta = \delta_0 + (\omega_q - \omega_p)\left(\frac{\beta_{2p} + \beta_{2q}}{2}\right). \tag{9}$$

We would now like to emphasize the fact that the importance of the contribution of the coherent coupling terms $\frac{1}{3}A_p^* A_q^2 \exp(2iz\Delta k)\exp(-2it\Delta\omega)$ and $\frac{1}{3}A_q^* A_p^2 \exp(-2iz\Delta k)\exp(2it\Delta\omega)$, in the right-hand sides of the NLSE (4) and (5), respectively, depends crucially on the value of the GVM [13,23]. For large GVM, these terms are usually considered as being negligible because they are rapidly varying. For small GVM, however, the wave vector mismatch decreases and their contribution must be investigated. As we shall see below, these terms only play a role in a very small parameter range which is outside the operating conditions of interest in the present paper. Consequently, throughout this section, we disregard the coherent coupling terms in the right-hand sides of the NLSE (4) and (5) and use the following equations:

$$\frac{\partial A_p}{\partial z} + \frac{1}{v_{gx,\omega_p}}\frac{\partial A_p}{\partial t} + \frac{1}{2}\, i\beta_{2p}\frac{\partial^2 A_p}{\partial t^2} = i\gamma_p\left(|A_p|^2 + \frac{2}{3}|A_q|^2\right)A_p, \tag{10}$$

$$\frac{\partial A_q}{\partial z} + \frac{1}{v_{gy,\omega_q}}\frac{\partial A_q}{\partial t} + \frac{1}{2}\, i\beta_{2q}\frac{\partial^2 A_q}{\partial t^2} = i\gamma_q\left(|A_q|^2 + \frac{2}{3}|A_p|^2\right)A_q, \tag{11}$$

that will be referred to as the ''ICE's'' (incoherently coupled equations). We will see later on that these ICE's give results which agree extremely well with the experimental data for large GVM. For small GVM the agreement is only qualitative but the prediction of the critical regime is effective. The benefit of using the ICE's is that the calculations required for obtaining the frequency spectra represent only a very small fraction of the amount of calculations required when using the NLSE (4) and (5). On the other hand, we would like to call the reader's attention to the fact that we do not investigate theoretically Raman effects in the present paper, although those effects are present in some experiments that will be presented in Sec. III.

B. Modulational instability conditions

Equations (10) and (11) admit the following steady state solution:

$$A_p = \sqrt{P}\exp[i\gamma_p(P + 2Q/3)z],$$
$$A_q = \sqrt{Q}\exp[i\gamma_q(Q + 2P/3)z]. \tag{12}$$

The linear stability of the steady state solution is examined by looking into the system in the presence of small amplitude and phase perturbations u and v; that is, we consider

$$A_p = (\sqrt{P} + u)\ \exp[i\gamma_p(P + 2Q/3)z],$$
$$A_q = (\sqrt{Q} + v)\ \exp[i\gamma_q(Q + 2P/3)z]. \tag{13}$$

Then, the linearization about $A_{p,q}$ yields

$$\frac{\partial u}{\partial z} - \frac{\delta}{2}\frac{\partial u}{\partial \tau} + \frac{i\beta_{2p}}{2}\frac{\partial^2 u}{\partial \tau^2} = i\gamma_p\left[P(u + u^*) + \frac{2}{3}\sqrt{PQ}(v + v^*)\right], \tag{14}$$

$$\frac{\partial v}{\partial z} + \frac{\delta}{2}\frac{\partial v}{\partial \tau} + \frac{i\beta_{2q}}{2}\frac{\partial^2 v}{\partial \tau^2} = i\gamma_q\left[Q(v + v^*) + \frac{2}{3}\sqrt{PQ}(u + u^*)\right], \tag{15}$$

$$\tau \equiv t - z\left[\frac{1}{2}\left(\frac{1}{v_{gx,\omega_p}} + \frac{1}{v_{gy,\omega_q}}\right)\right].$$

Then we assume for the perturbation a modulational ansatz with wave number K and frequency Ω, of the form

$$u = u_s\exp[i(\Omega\tau - Kz)] + u_a\exp[i(-\Omega\tau + Kz)], \tag{16}$$

$$v = v_s\exp[i(\Omega\tau - Kz)] + v_a\exp[i(-\Omega\tau + Kz)], \tag{17}$$

where u_s and u_a can be regarded, respectively, as the measures of the amplitudes of the Stokes and anti-Stokes sidebands for the fast axis, whereas v_s and v_a represent the Stokes and anti-Stokes sidebands for the slow axis.

Substitution of Eqs. (16) and (17) into Eqs. (14) and (15) leads to the following eigenvalue equation:

$$[M][Y] = K[Y], \tag{18}$$

where the eigenvector is defined as

$$[Y]^T \equiv [u_a, u_s^*, v_a, v_s^*], \tag{19}$$

$[M]$ is the stability matrix of the system,

$$[M]\equiv\begin{pmatrix} -\frac{\Omega\delta}{2}+\beta_{2p}\frac{\Omega^2}{2}+\gamma_p P & \gamma_p P & \frac{2}{3}\gamma_p\sqrt{PQ} & \frac{2}{3}\gamma_p\sqrt{PQ} \\ -\gamma_p P & -\frac{\Omega\delta}{2}-\beta_{2p}\frac{\Omega^2}{2}-\gamma_p P & -\frac{2}{3}\gamma_p\sqrt{PQ} & -\frac{2}{3}\gamma_p\sqrt{PQ} \\ \frac{2}{3}\gamma_q\sqrt{PQ} & \frac{2}{3}\gamma_q\sqrt{PQ} & \frac{\Omega\delta}{2}+\beta_{2q}\frac{\Omega^2}{2}+\gamma_q Q & \gamma_q Q \\ -\frac{2}{3}\gamma_q\sqrt{PQ} & -\frac{2}{3}\gamma_q\sqrt{PQ} & -\gamma_q Q & \frac{\Omega\delta}{2}-\beta_{2q}\frac{\Omega^2}{2}-\gamma_q Q \end{pmatrix}, \quad (20)$$

from which we obtain the following dispersion relation:

$$\det([M]-K[I])=0. \quad (21)$$

The MI phenomenon occurs when the wave number K of the perturbation possesses a nonzero imaginary part, by an exponential growth of the amplitude of the perturbation. The importance of the phenomenon is measured by a power gain G defined by

$$G(\omega)\equiv 2|\mathrm{Im}(K)|. \quad (22)$$

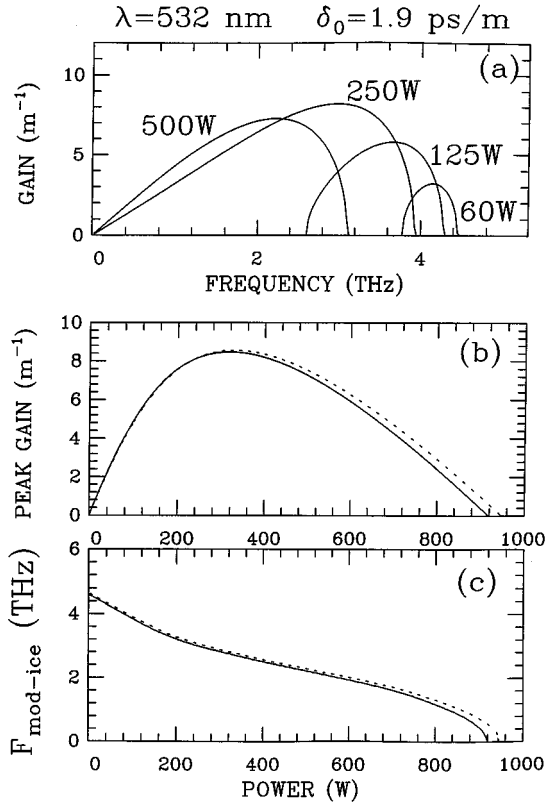

FIG. 1. Single-frequency-copropagation regime at λ=532-nm wavelength (GVM δ_0=1.9 ps/m) and the same input-wave power P for each birefringence axis. (a) MI gain vs frequency for P=500, 250, 125, and 60 W. (b) MI peak gain vs power P (solid curve). (c) Optimum modulation frequency $F_{\text{mod-ICE}}$ vs power P (solid curve). In (b) and (c), the dotted curves represent the results for the two-frequency-copropagation regime of GVM $\delta=-\delta_0$, which is discussed in Sec. II D.

We have found out that the phenomenon manifests itself in qualitatively different ways depending on whether the two copropagating waves vibrate at the same frequency or not. For the sake of clarity, we discuss the two cases separately.

C. Single-frequency-copropagation regime

In this subsection we briefly review a particularly interesting case that occurs when the input-wave power is equally distributed along the two birefringence axes, for a single-frequency-copropagation regime, that is, $P=Q$. Indeed, in this case, $\gamma\equiv\gamma_p=\gamma_q$, $\beta_2\equiv\beta_{2p}=\beta_{2q}$; which leads to the following expression for the dispersion relation (21):

$$K^2=\rho+\xi^2\pm[(\rho+\xi^2)^2+C^2-(\rho-\xi^2)^2]^{1/2}, \quad (23)$$

$$\rho\equiv\tfrac{1}{2}\beta_2\Omega^2(\tfrac{1}{2}\beta_2\Omega^2+2\gamma P), \quad (24)$$

$$C\equiv\tfrac{2}{3}\Omega^2(P\gamma\beta_2), \quad (25)$$

$$\xi\equiv\tfrac{1}{2}\Omega\delta. \quad (26)$$

We recall that in this copropagation regime, the GVM reduces to $\delta_0=B/c$. So, Eq. (23) yields the condition for the MI phenomenon to occur, that is,

$$C^2-(\rho-\xi^2)^2>0. \quad (27)$$

Figures 1(a), 1(b), and 1(c) show, respectively, the gain spectra for different powers, the peak gain vs power P, and the optimum modulation frequency—defined as the frequency at which the gain attains its maximum value and denoted $F_{\text{mod-ICE}}$ in Fig. 1(c). These figures have been obtained for a pump wave at 532-nm wavelength, propagating in an optical fiber with a birefringence $B=5.7\times10^{-4}$, which corresponds to the following parameter values: δ_0=1.9 ps/m, γ=44.9 $\mathrm{W^{-1}\,km^{-1}}$, and β_2=65.69 $\mathrm{ps^2\,km^{-1}}$.

As a general result, one finds out that the MI phenomenon manifests itself in Ω-frequency regions which depend on the input-wave power level. The following table summarizes the different cases:

Power domain	Instability domain
$P<P_0$	$\Omega_0<\Omega<\Omega_c$
$P_0<P<P_c$	$\Omega<\Omega_c$
$P>P_c$	no MI

where

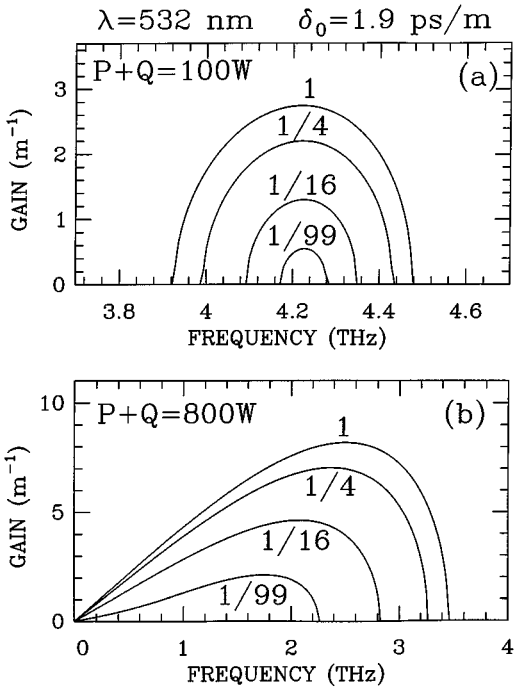

FIG. 2. MI gain vs frequency for the single-frequency-copropagation regime at 532-nm wave-length, for different values of the ratio of the input power on the fast axis P related to the input power on the slow axis Q but with a constant total power $P+Q$. The curves correspond to different values of the ratio P/Q of 1, 1/4, 1/16, and 1/99. (a) $P+Q=100$ W. (b) $P+Q=800$ W.

$$P_0=\frac{3\delta_0^2}{20\gamma\beta_2},\quad P_c(\omega_p=\omega_q)\equiv\frac{3\delta_0^2}{4\gamma\beta_2}, \tag{28}$$

$$\Omega_c^2\equiv(2\pi f_c)^2=\left(\frac{\delta_0}{\beta_2}\right)^2-\frac{4\gamma P}{3\beta_2}, \tag{29}$$

$$\Omega_0^2\equiv(2\pi f_0)^2=\left(\frac{\delta_0}{\beta_2}\right)^2-\frac{20\gamma P}{3\beta_2}, \tag{30}$$

Ω_c and Ω_0 are, respectively, the high and low cutoff frequencies, P_0 is the power at which the low cutoff frequency becomes zero, and P_c is the critical power beyond which the MI phenomenon disappears.

The results in Fig. 1 are similar to those obtained by Rothenberg [20], except very slight differences in the instability regions as well as in the amplitude of peak gain, which are simply due to the difference in the fiber parameters. We see in Fig. 1(a) that the unstable frequency regions get narrower as the power decreases, and in the limit of low power, reduce to an OMF (optimum modulation frequency) $F_{\text{mod-ICE}}=\Omega_c/2\pi\approx\Omega_0/2\pi\approx(1/2\pi)(\delta_0/\beta_2)=4.6$ THz. Figure 1(b) shows that the peak-gain power dependence exhibits a maximum at $P=318$ W, and then decreases and vanishes as soon as P exceeds the critical power $P_c=918$ W. Figure 1(c) shows that the OMF decreases monotonically to zero as P increases.

The case just considered, $P=Q$, is particularly interesting because the MI gain attains its maximum when the input-wave power is equally distributed between the two birefringence axes. This appears clearly in Fig. 2, obtained by solving numerically the dispersion relation (21), and where the sideband is represented for different values of the ratio P/Q but with constant total power $P+Q$. Figures 2(a) and 2(b) correspond, respectively, to $P+Q=100$ and 800 W. We see, as expected for an optical fiber in the normal dispersion regime, that MI progressively vanishes when an increasingly large part of the total input power is introduced on one birefringence axis and only a small fraction on the other axis. Moreover we note in Fig. 2(a) that the OMF does not depend significantly on the power ratio P/Q ($F_{\text{mod-ICE}}\approx4.22$ THz). As we shall see in Sec. III, this peculiar feature has been verified experimentally. This result shows that the analytical solution obtained in Eq. (23) for $P=Q$ can also be used for quickly obtaining a good estimation of the OMF for $P\neq Q$, provided that the total input power $P+Q$ is not too large. On the other hand, we see in Fig. 2(b) that at higher power, the OMF varies significantly with respect to the polarization of the input waves, which implies that one can no longer use Eq. (23) for approximating the OMF for $P\neq Q$.

We conclude this subsection by pointing out the particularly important feature that the critical power P_c [see Eq. (28)] beyond which MI disappears never becomes zero in the single-frequency-copropagation regime. This implies that in a highly birefringent fiber, if two waves, orthogonally polarized, copropagate with the same frequency, there will always exist a range for the input-wave power in which MI will appear. The question then arises as to whether the system exhibits the same type of behavior when the two waves copropagate at different frequencies.

D. Two-frequency-copropagation regime

In this subsection we consider the system in the presence of two waves copropagating at different wavelengths, λ_p (along the fast axis) and λ_q (along the slow axis). This copropagation regime is particularly interesting because of the possibility to vary the GVM. Equation (9) shows that this variation can be achieved by just varying the wavelength separation between the two pump waves. We have obtained a description of the system by solving the general dispersion relation (21). The system exhibits qualitatively different features depending on the value of the GVM. For clarity we present the different cases separately.

1. ICE study for large positive GVM: $\delta\gg\delta_0$

A typical example of the system behavior for large positive GVM is shown in Fig. 3, obtained for $\lambda_q=532$ nm and different values for λ_p, by using the same input power $P=Q$ for each birefringence axis. The wavelength λ_p is chosen larger than λ_q in such a way that, due to the normal dispersion, the GVM is larger than δ_0 [see Eq. (9)]. The chosen wavelength pairs (λ_p,λ_q) correspond in fact to those which have been used in some experiments that will be presented in Sec. III. We see in Fig. 3(a) that the peak gain is, for the same input power, much larger than for the single-frequency copropagation [Figs. 1(a) and 1(b)]. But the greatest qualitative difference in Fig. 3 comes from the critical-power levels, which are two orders of magnitude larger than in the single-frequency case illustrated in Fig. 1. These high-power levels, in Fig. 3, are of course unpractical with an optical fiber as nonlinear medium. In fact only the low-power region (less

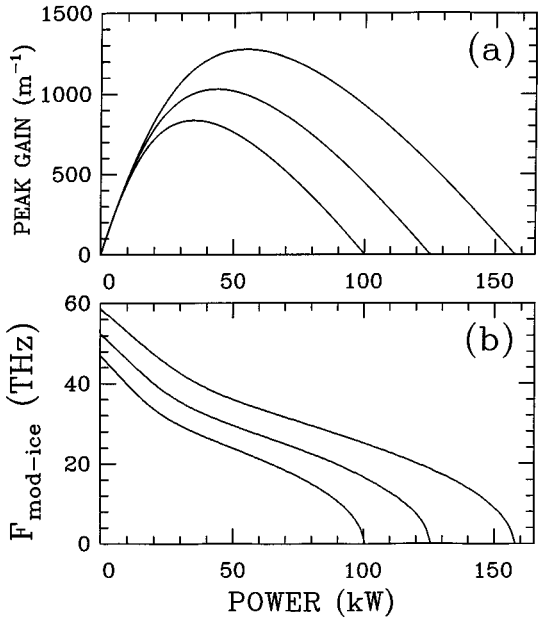

FIG. 3. Two-frequency-copropagation regime for large GVM and the same input power for each birefringence axis. The curves correspond (from the largest to the smallest) to the wavelength pairs ($\lambda_p=588$ nm, $\lambda_q=532$ nm), ($\lambda_p=581$ nm, $\lambda_q=532$ nm), and ($\lambda_p=575$ nm, $\lambda_q=532$ nm). The corresponding GVM's are, respectively, $\delta=22.6640$, 20.4300, and 18.4420 ps/m. (a) MI gain vs power P. (b) OMF vs power P.

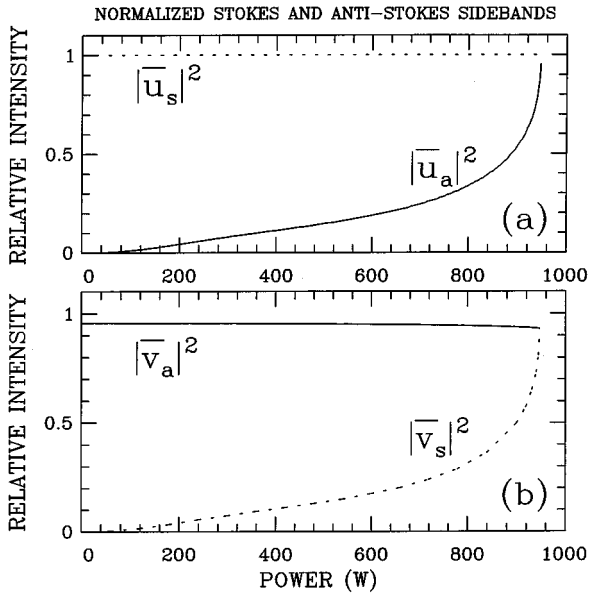

FIG. 4. Eigenvectors of the system for the two-frequency-copropagation regime with $\delta=-\delta_0$. The curves correspond to the intensities of the sidebands, normalized to the highest intensity of the four sidebands: $|\overline{u_{a,s}}|^2\equiv|u_{a,s}|^2/\text{Max}(|u_a|^2,|u_s|^2,|v_a|^2,|v_s|^2)$, $|\overline{v_{a,s}}|^2\equiv|v_{a,s}|^2/\text{Max}(|u_a|^2,|u_s|^2,|v_a|^2,|v_s|^2)$.

than 1 kW) corresponds to power levels that can be reached in a fiber. Nevertheless, the important point in Fig. 3 is the indication that at high GVM the MI gain is large and the critical power is well above any practical power level; which implies that practical situations in which $\delta \gg \delta_0$ might be extremely favorable for monitoring MI in a highly birefringent fiber.

Furthermore we see in Fig. 3(b) that at low power the MI frequencies are much larger than in the case of Fig. 1(c). For example, we see in Fig. 3(b), for the wavelength pair ($\lambda_q=532$ nm, $\lambda_p=581$ nm), that the OMF for $P=9$ W appears at $F_{\text{mod-ICE}}=52.41$ THz. It is interesting to note that the eigenvector corresponding to the unstable eigenvalue in this situation is given by $[u_a,u_s^*,v_a,v_s^*]=[0.46+0.75i,0,0,-0.57+0.82i]$. This expression reveals that the whole system with two pump waves ($\lambda_q=532$ nm, $\lambda_p=581$ nm) generates in fact only two sidebands: an anti-Stokes sideband u_a on the fast axis, and a Stokes sideband v_s on the slow axis. Moreover, knowing that the wavelength pair ($\lambda_q=532$ nm, $\lambda_p=581$ nm) corresponds to a frequency difference $(1/2\pi)(\omega_q-\omega_p)=47.56$ THz, it becomes clear that the Stokes sideband developed on the slow axis appears at $52.41-47.56=4.85$ THz below ω_p, whereas the anti-Stokes sideband developed on the fast axis appears at 4.85 THz above ω_q. This shows that at low power, for large positive GVM, MI generates two sidebands, which takes place outside the frequency interval between the two pump waves. All these general features are verified for all practical power levels in the fiber (less than 1 kW). Indeed we see in Fig. 3(b) that the OMF varies only very slightly in this power region.

2. ICE study for $\delta=-\delta_0$

We consider the particular situation in which the wavelength pair (λ_p,λ_q) is such that the GVM is equal to that of the single-frequency-copropagation regime but with opposite sign $\delta=-\delta_0$. In this case then, the wavelength λ_p is smaller than λ_q so that the group velocity on the fast axis becomes larger than that on the slow axis. We have verified that the wavelength pair ($\lambda_p=532$ nm, $\lambda_q=540.9310$ nm) yields $\delta=-\delta_0=-1.9$ ps/m. This situation is illustrated by the dotted curves in Figs. 1(b) and 1(c) [note that the dotted curve in Fig. 1(c) corresponds in fact to the magnitude of the OMF]. As can be easily shown from the symmetries of the stability matrix $[M]$, Eq. (20), the sign of δ does not affect the magnitude of the MI frequency. The slight differences observed in Figs. 1(b) and 1(c) are due to the differences in nonlinear coefficients and dispersions, which for the wave λ_q are now $\gamma_q=43.03$ W^{-1} km^{-1} and $\beta_q=64.24$ ps^2 km^{-1}, which are slightly different from $\gamma=44.9$ W^{-1} km^{-1} and $\beta_2=65.69$ ps^2 km^{-1}.

Therefore it becomes clear that for a given input power the GVM is really the *control parameter* that governs the MI phenomenon in the system, in the sense that the variation of this parameter can be used for obtaining the operating conditions of the system including, in particular, the phenomena observed in the single-frequency-copropagation regime. Note on the other hand that as shown in Figs. 1(b) and 1(c), the single- and two-frequency-copropagation regimes for GVM of magnitude 1.9 ps/m exhibit general features similar to those mentioned above for large GVM, except two major points: first, the critical power is significantly reduced compared to the critical-power levels in Fig. 3. Second, the eigenvectors of the system, which are shown in Fig. 4, reveal that MI generates four sidebands at power levels which are accessible in an optical fiber, contrary to the large δ case

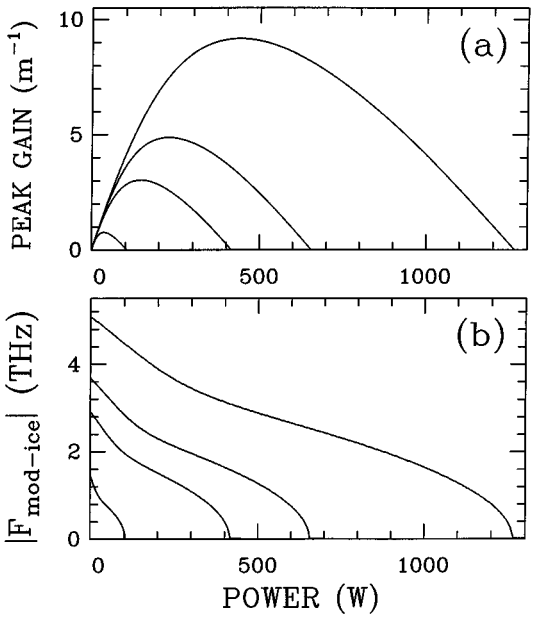

FIG. 5. Two-frequency-copropagation regime for $\lambda_p = 576$ nm, small positive and negative GVM, with the same input power on each birefringence axis. The curves correspond (from the largest to the smallest) to the wavelength pairs ($\lambda_p = 576$ nm, $\lambda_q = 587.6$ nm), ($\lambda_p = 576$ nm, $\lambda_q = 577.6$ nm), ($\lambda_p = 576$ nm, $\lambda_q = 585.1$ nm), and ($\lambda_p = 576$ nm, $\lambda_q = 580.1$ nm). The corresponding GVM's are, respectively, $\delta = -1.8630$, 1.3658, -1.0730, and 0.5411 ps/m. (a) MI peak gain vs power P. (b) OMF vs power P.

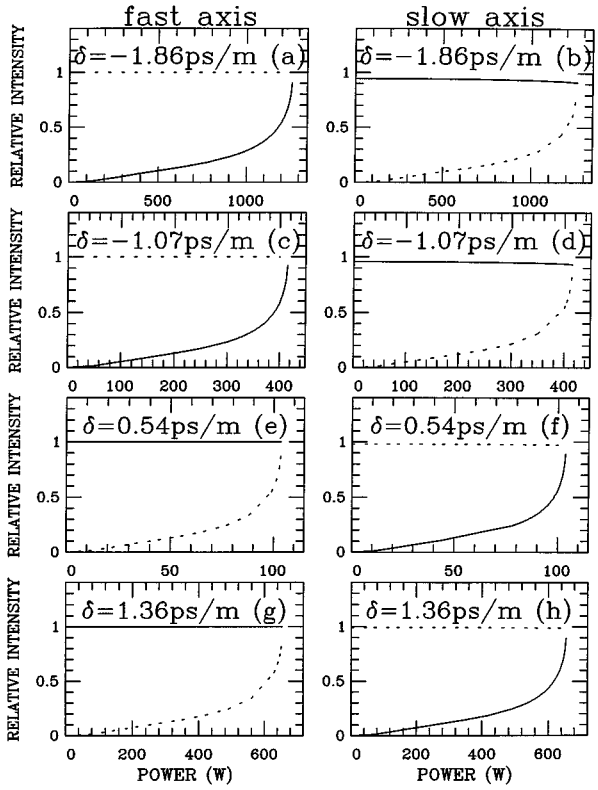

FIG. 6. Eigenvectors of the system for the two-frequency-copropagation regime considered in Fig. 5. The solid curves correspond to anti-Stokes waves, and the dotted curves to Stokes waves.

considered previously where only two sidebands were generated. More specifically, the two following points emerge from the analysis of the case $\delta = -\delta_0$ shown in Fig. 4: first, we see that for sufficiently low-power levels (compared to the critical power), $u_a \approx v_s \approx 0$, thus indicating that MI generates a Stokes sideband u_s on the fast axis on which the pump wave has the highest frequency ω_p, and an anti-Stokes sideband v_a on the slow axis. The second point is that as the input power increases the importance of the sidebands u_a and v_s becomes less and less negligible. As a matter of fact when the power approaches the critical power, the magnitudes of these sidebands increase abruptly until becoming exactly equal to the intensities of the sidebands u_s and v_a that were initially prominent. In conclusion, our analysis of the eigenvectors of the stability matrix reveals that the individual contributions of the four sidebands to the frequency spectrum of the system depends crucially on the input power level. Note that although it has not yet been previously recognized, this fundamental feature also characterizes MI in the single-frequency-copropagation regime considered in Refs. [20–22].

3. ICE study for $\lambda_p = 576$ nm and $|\delta| < \delta_0$

Figure 5 shows the results that we have obtained by taking the same wavelength pairs ($\lambda_p = 576$ nm, λ_q) as those used in some experiments that are presented in Sec. III. At first glance this figure exhibits the same general features as those mentioned previously. In particular, we observe that the critical-power level decreases significantly as $|\delta|$ decreases. However, a careful examination of the eigenvectors of the system reveals some fundamental differences that become clearly apparent in Fig. 6. We see in Figs. 6(a)–6(d), which correspond to negative δ values, that the system exhibits the same type of distribution of sidebands in the frequency spectrum as for the case $\delta = -\delta_0$ considered in Fig. 4. Indeed, for low-power levels one verifies $u_a \approx v_s \approx 0$. The subsequent frames reveal that when δ changes sign the Stokes and anti-Stokes sidebands interchange their role. Thus when δ is negative the sideband frequencies are located between the two pump frequencies, contrary to the case of positive GVM where the sidebands lie outside this interval.

Furthermore, there exist some other fundamental differences in the small-δ region, as illustrated in Fig. 7. Each point of the curves in Figs. 7(a) and 7(b) represents the critical power corresponding to a wavelength pair (λ_p, λ_q), where two fixed values of λ_p are considered: $\lambda_p = 532$ and 576 nm, respectively. The critical-power curve $P_c(\lambda_q)$, which has the shape of a parabola, exhibits a minimum of zero power at a wavelength, say λ_q^0. This critical-power curve then divides the parameter plane into three regions. The region above the curve represents modulationally stable operating conditions, while the two regions below the curve on each side of λ_q^0 represent the conditions of occurrence of MI. This feature can be easily explained from Eq. (9) which shows that there exist pairs of pump frequencies (or wavelengths) for which the GVM is equal to zero. As in the single-frequency configuration, when $\delta = 0$ the critical power vanishes [see Eq. (28) which shows the parabolic dependence of P_c as a function of δ_0 for the single-frequency case]. Figures 7(c) and 7(d) show that when $\lambda_p = 532$ nm, the

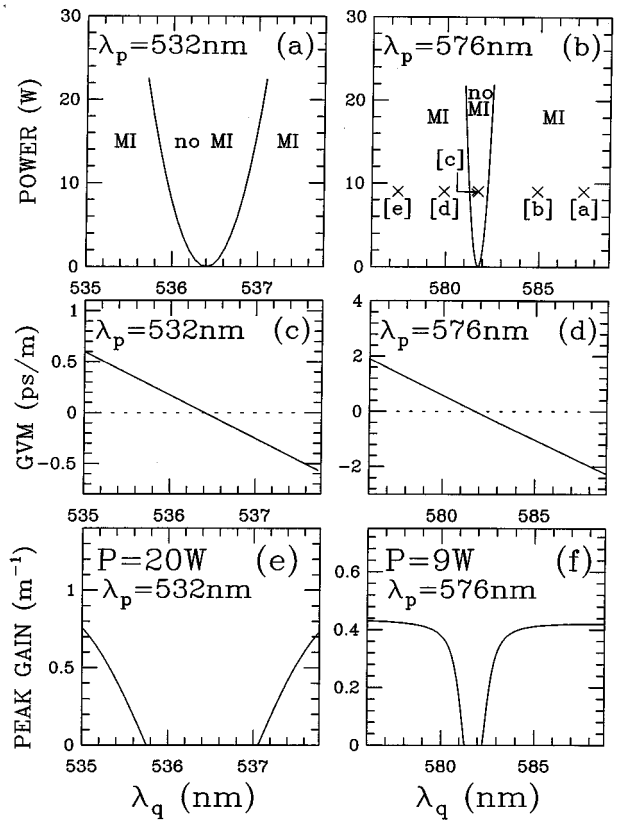

FIG. 7. Plot showing the critical regime for the two-frequency-copropagation regime, where the same input power is applied in each birefringence axis. (a), (b) Each point (λ_p, λ_q, $P=Q$) of the parameter region considered corresponds to a parameter set required for performing a two-frequency copropagation, and the solid curve represents the critical power P_c vs λ_q wave-length, for $\lambda_p=532$ and 576 nm, respectively. The crosses in (b) correspond to operating conditions used for obtaining the experimental results in Fig. 13, which are discussed in Sec. III C. (c), (d) GVM vs λ_q. (e), (f) Peak gain vs λ_q.

value of λ_q which satisfy $\delta=0$ is $\lambda_q^0=536.41$ nm, and for $\lambda_p=576$ nm we have $\lambda_q^0=581.75$ nm. These λ_q^0 values correspond to the minima of the critical-power curves of Figs. 7(a) and 7(b). This analysis shows that the critical regime can be reached at arbitrarily small powers in the two-frequency-copropagation regime, contrary to the single-frequency regime which requires unpractical powers since δ_0 is large and cannot be varied. This extra flexibility explains how the use of two frequencies in the highly birefringent fiber allowed us to observe experimentally the critical regime of MI, that will be presented in Sec. III.

The behavior shown in Figs. 7(a) and 7(b) can also be understood in the following way: when varying λ_q at a given power level $P=Q$ in the fiber, the features described above will appear in the form of a sort of ''critical gap,'' in which MI will disappear. This is illustrated in Figs. 7(e) and 7(f), which give the peak gains for two power levels ($P=20$ and 9 W) for the case of Figs. 7(a) and 7(b), respectively. These curves show that the peak gain undergoes an abrupt drop to zero as one approaches the critical gap. Another interesting feature to be emphasized is that the size of the critical gap, which is the distance that separates (for a given power P) the two branches of each critical-power curve in Figs. 7(a) and 7(b), continuously decreases as the input power decreases, until going asymptotically to zero when the wave power tends to zero. In general, some care must be taken in the experimental study of the general features described above, i.e., in monitoring the *critical gap* or *critical regime* in real systems. Indeed, because of the fiber losses, the waves which are launched in the fiber in the critical gap, that is, with a power above the critical power, will see their power decreasing. This power decrease corresponds, in Figs. 7(a) and 7(b), to a vertical displacement towards the low-power region, that may intersect the critical-power curve, thus leading to a transition to the MI regime. Consequently, a system which is initially in the critical gap might become modulationally unstable because of fiber loss. This shows that the fiber length is a crucial parameter in the experimental observation of the critical regime. A system of two waves will remain in the critical gap only if the fiber length is sufficiently small; otherwise (if the fiber length is very large) the system will always end up by making transition to the MI regime. However, if the pump wavelengths are chosen in such a way that the system has a zero critical power, that is, $\lambda_q=\lambda_q^0$, then the two waves will propagate throughout the fiber without ever undergoing transition to the MI regime, whatever the fiber length and the input-wave power. Thus the wavelength separation $\Delta\lambda\equiv\lambda_p-\lambda_q$, which determines the GVM, appears as a crucial parameter for the two-frequency copropagation in highly birefringent fibers. The physical situation corresponding to the particular wavelength pairs (λ_p,λ_q^0) appears to be potentially interesting for copropagating two waves without MI, that is, in highly stable conditions for any input-wave power and fiber length, in the normal dispersion regime.

We would now like to reemphasize that all results presented so far have been obtained via ICE's that neglect coherent coupling terms by invoking the fact that the wave vector mismatch Δk is sufficiently large. This assumption is valid for the single-frequency copropagation, as we will see below, but for the two-frequency copropagation the wave vector mismatch may become small, at least in some parameter ranges; their role must therefore be investigated. This can be easily done by evaluating the value of the wave vector mismatch Δk as a function of the wavelength difference $\Delta\lambda\equiv\lambda_q-\lambda_p$ which constitutes the control parameter in our experiments. When Δk is sufficiently large the coherent coupling terms rapidly vary and can therefore be neglected. More precisely, if the beat length $L_B\equiv 2\pi/\Delta k$ is short compared to the fiber length over which MI takes place the coherent coupling terms can be neglected in a good approximation. We evaluate Δk by means of the following procedure: we assume that the intrinsic birefringence is independent of the wavelength, so that the wave vectors k_x and k_y can be written as $k_x(\omega)=(\omega/c)[n(\omega)-B/2]$ and $k_y(\omega)=(\omega/c)[n(\omega)+B/2]$, where $n(\omega)$ is the effective refractive index of the fiber. This index can be evaluated in a first approximation from the material's Sellmeier coefficients (i.e., we neglect the waveguide dispersion). The results are represented in Fig. 8 where we plotted L_B as a function of the wavelength λ_q, for $\lambda_p=532$ and 576 nm, respectively. Quite remarkably we see that L_B takes large values only in a small wavelength range $\Delta\lambda_q<0.5$ nm, located very close to the fixed λ_p wavelength. In the two examples above, L_B attains its maximum value, which is well above 0.2 m, when

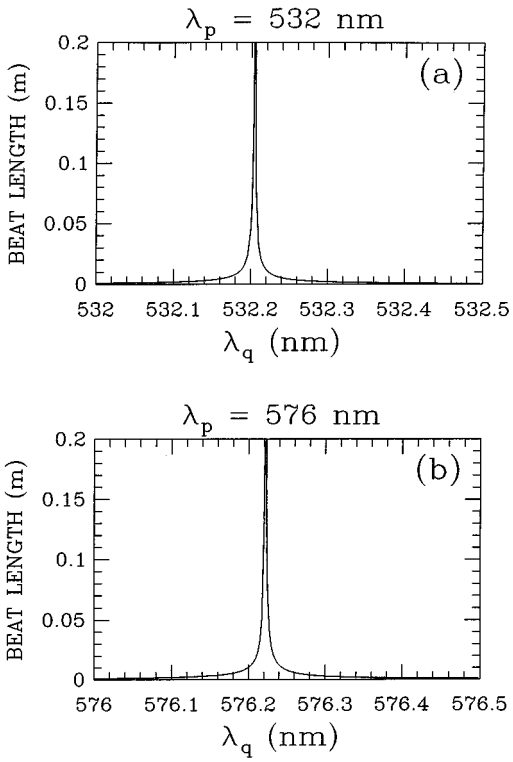

FIG. 8. Plot showing the beat length vs λ_q for (a) $\lambda_p = 532$ nm and (b) $\lambda_p = 576$ nm.

$\lambda_q - \lambda_p \approx 0.2$ nm. This result shows that the coherent coupling terms enter into play only for small wavelength separations between the two pump waves, and in a small wavelength region whose size is in fact closely related to the fiber length. As we shall see in Sec. III, this peculiar feature can be easily verified experimentally. On the other hand, the particular case $\lambda_p = \lambda_q$ (single-frequency regime) corresponds to a beat length whose value is less than 10^{-3} m in the two examples in Fig. 8, which indicates clearly that the effects of the coherent coupling terms are then negligible for a fiber length of 19 m. Note also that the wavelength pair (λ_p, λ_q^0), which corresponds to $\delta = 0$, is well far away from the parameter regions considered in Figs. 8(a) and 8(b), and therefore Figs. 8(a) and 8(b) give evidence that the coupling terms are well negligible for small GVM between the two pump waves.

In conclusion, from this simple analysis, we can state that the ICE model is valid in a very wide parameter range, and in particular, in the parameter regions considered in our experiments in Sec. III.

We conclude this subsection by pointing out that although the ICE's have provided deep insight into the problem of MI in the highly birefringent fiber, the analysis of these equations does not provide a complete picture of all aspects of the problem. In the following subsection we develop a complementary approach to the problem, that is, we describe and interpret MI in the base of a discussion of the phase-matching conditions of the four-wave-mixing processes underlying MI.

E. Phase-matching conditions

It is interesting to interpret the features described above by means of the phase-matching conditions of the four-wave-mixing (FWM) processes responsible for MI. As we shall see below, the FWM picture provides a better understanding of the physics underlying MI in the highly birefringent fiber. It also provides analytical expressions for the functional dependence of the OMF in terms of the frequency difference $(\omega_q - \omega_p)$ which was not available from the ICE approach. Let us first consider the phase-matching conditions in the linear limit case, that is, we neglect the role of the nonlinear index modulation with respect to the large linear index difference due to the linear birefringence. In this approximation, considering the FWM process $\omega_p + \omega_q - (\omega_p + \Omega) - (\omega_q - \Omega)$ (which involves the two prominent sidebands) leads to the following expression of the phase mismatch [24]: $\Delta k_L \equiv -\delta\Omega + \Omega^2(\beta_{2p} + \beta_{2q})/2$. The first term of the right-hand side represents the role of the GVM between the two waves, Eq. (9), while the second term represents the role of the dispersion. In this approximation, the phase-matching condition $\Delta k_L = 0$ provides the following expression of the OMF:

$$\Omega_{\text{opt-}l} \equiv \frac{2\delta}{\beta_{2p} + \beta_{2q}}. \tag{31}$$

In the particular case $\omega_p = \omega_q$ this value becomes the cutoff frequency given in Eq. (29) in the low-power limit. In general, the above situation can be easily interpreted as follows: the FWM occurs when the effect of GVM on the sideband waves is exactly compensated by dispersion (the larger the dispersion the smaller the OMF). Using the expression (9) of δ one can write the OMF in terms of the frequency difference between the two pump waves:

$$\Omega_{\text{opt-}l} = \frac{2\delta_0}{\beta_{2p} + \beta_{2q}} + \omega_q - \omega_p. \tag{32}$$

The functional dependence of $\Omega_{\text{opt-}l}/2\pi$ upon the wavelength pairs ($\lambda_p = 576$ nm, λ_q) is represented by the dotted curve in Fig. 9.

Let us now consider the role of the nonlinearity in the phase-matching condition. From a simple analysis of the ICE's one finds that the nonlinear contribution to the phase mismatch is given by [24]

$$\Delta k_{\text{nl}} = P\gamma_p + Q\gamma_q.$$

The phase-matching condition is now written $-\delta\Omega + [(\beta_{2p} + \beta_{2q})/2]\Omega^2 + P\gamma_p + Q\gamma_q = 0$, which leads to the following expression for the OMF:

$$\Omega_{\text{opt-nl}} \equiv \frac{\delta \pm \sqrt{\delta^2 - 2(\beta_{2p} + \beta_{2q})(\gamma_p P + \gamma_q Q)}}{\beta_{2p} + \beta_{2q}}. \tag{33}$$

Using Eq. (9) this expression provides the OMF as a function of the frequency difference $\Delta\omega$, or equivalently, as a function of λ_q for a given value of λ_p. The result is represented by the solid curve in Fig. 9. As can be seen from Eq. (33), the OMF becomes complex when $|\delta| < [2(\beta_{2p} + \beta_{2q})(P\gamma_p + Q\gamma_q)]^{1/2}$. In other words, the nonlinearity is

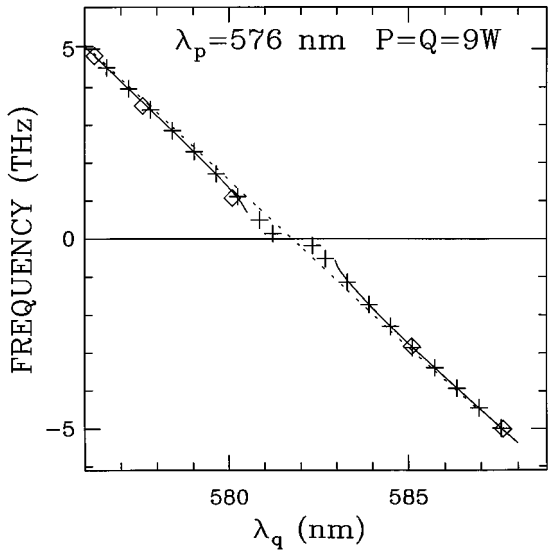

FIG. 9. Plot showing the role of the nonlinearity in the phase-matching condition of the FWM process for $\lambda_p = 576$ nm, $P = Q = 9$ W, and λ_q in the range 576 nm$\leqslant\lambda_q\leqslant$589 nm. The dotted curve represents $\Omega_{\text{opt-l}}/2\pi$, Eq. (32). The solid curve represents $\Omega_{\text{opt-nl}}/2\pi$, Eq. (33). The + symbols represent the OMF obtained via the dispersion relation, Eq. (21). The centers of the diamonds represent some experimental results that will be presented in Sec. III.

responsible for the presence of a frequency gap in the MI spectrum. Thus this nonlinearity induced gap is at the origin of the critical regime described in the preceding subsection. Note that the analytical expression of Eq. (33) provides a rather good approximation of the OMF. Comparison with the exact OMF derived from the ICE's is given in Fig. 9 where the + symbols represent the results obtained via the linear stability analysis of the ICE's. The meaning of the diamond symbols, Fig. 9, will be given in the following section.

III. EXPERIMENTAL STUDY

A. Experimental setup

In our experiments, MI is induced by a nonlinear coupling between the two orthogonally polarized waves propagating in a strongly birefringent fiber without introducing any initial perturbation. In the single-frequency case both waves come from a Nd:YAG (YAG denotes yttrium aluminum garnet) laser, and in the two-frequency case the two waves are produced, respectively, by a Nd:YAG and a dye laser. We will describe the experimental setup in its more general configuration, that is, with two lasers. The simplified schematic of the experimental setup is shown in Fig. 10. The MI is generated by the interaction of a Nd:YAG beam and a dye amplified beam. On one hand, the Nd:YAG is the Quanta Ray model GCR-3 made up of a master oscillator which can be injection seeded by a Quanta Ray model 6300 diode laser. After doubling its frequency in a nonlinear potassium dihydrogen phosphate (KDP) crystal, transform-limited pulses of approximately 7-ns duration are obtained at 532-nm wavelength, which provide peak powers of several MW. When the laser is injection seeded it has a spectral resolution of 3.7×10^{-3} cm^{-1}. The spectral resolution reduces to about 1

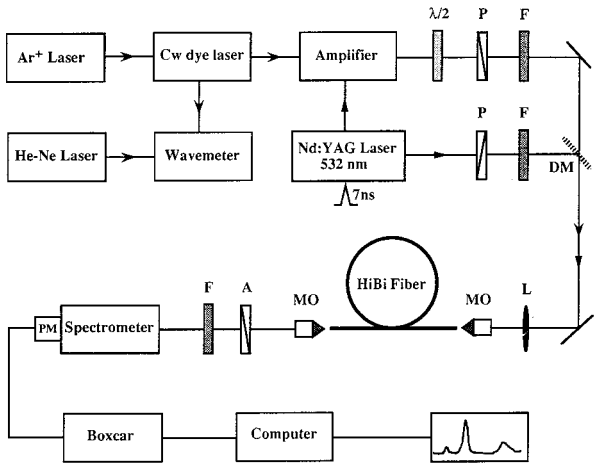

FIG. 10. Schematic diagram of the experimental apparatus. *P*: Glan-Foucault polarizer, *F*: neutral filter, DM: dichroïc mirror, *L*: steering lens, MO: microscopic objective, *A*: Glan-Foucault analyzer, PM: photomultiplier, HiBi Fiber: high birefringent fiber.

cm^{-1} when it is multimode. On the other hand, the tunable dye laser is the Spectra Physics model 380 frequency stabilized ring dye laser pumped by a 4-W argon laser. This dye laser passes through a home built three stage dye cell amplifier, transversally pumped by a second part of the Nd:YAG laser. The linewidth of the resulting tunable laser is nearly limited by the Fourier transform of its pulse width and is equal to 3.7×10^{-3} cm^{-1} [25,26]. Its wavelength was tuned between 575 and 588 nm and measured by a cw wavemeter [27]. The peak powers used in this experiment range between 10 and 100 W for both lasers.

A $\lambda/2$ plate and two Glan-Foucault polarizers (extinction of the opposite wave 10^5:1) followed by a set of filters allow one to obtain a pair of orthogonally polarized pulses with adjustable intensities. The two beams are then combined by a dichroic mirror. The YAG and dye beams are focused with a steering lens (focal length 50 cm) and with a microscopic objective (focal length 4.3 mm). The steering lens of the coupler is positioned near the back focus, so a transverse translation of this lens causes a much smaller translation of the focused spot (in the ratio of the focal lengths of the two lenses). As a consequence, the steering lens greatly facilitates the alignment of the fiber to the incoming beams. The strongly birefringent fiber is the HB600 fiber from Fibercore Ltd. It has a quoted beat length of 1.11 mm at 633 nm, a cutoff wavelength of 507 nm, an attenuation of 13 dB/km at 633 nm, and a length of 19 m. The optimum launch spot size is 3 μm. In our experiments the expected modulation period is less than 220 fs, the pulse duration is about four orders of magnitude larger than the modulation period, and therefore the pulses provide a quasi-cw condition. The advantage of nanosecond pulses with respect to picosecond pulses is to increase significantly the overlap time, and the interaction length is primarily limited by optical losses in the visible domain. At the fiber output, the beam is collimated and sent into a 50-cm spectrometer (SPEX 1301), which allows us to record the modulation frequency with high resolution (1 cm^{-1}). A third Glan-Foucault polarizer selects the output light propagating along the fast and the slow axis, and so selects the YAG or dye beam. The YAG and dye beam pow-

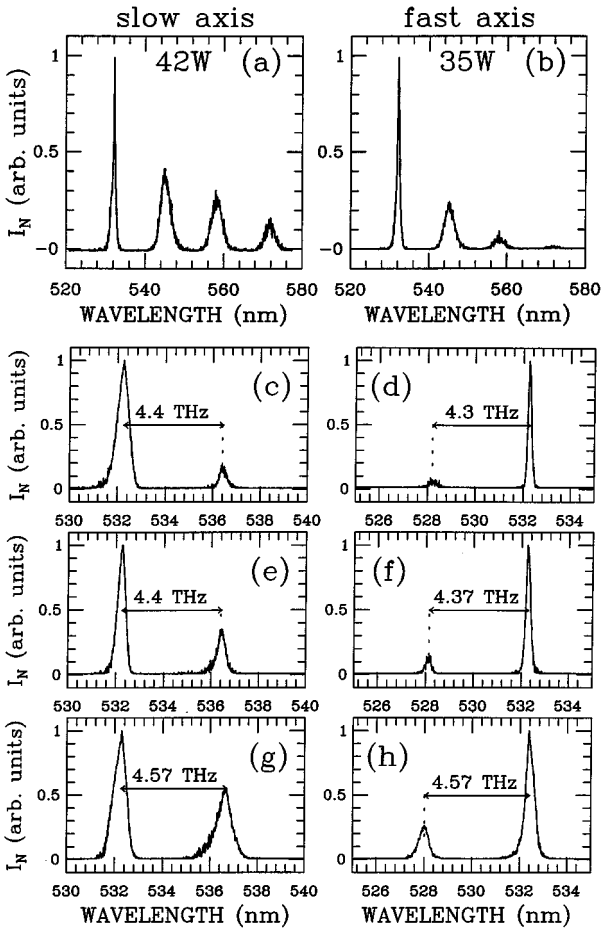

FIG. 11. Spectra of light emerging from the slow axis [(a), (c), (e), (g)] and the fast axis [(b), (d), (f), (h)] of the fiber for the single-frequency-copropagation regime, for increasing polarization (with respect to the slow axis). The pump wave operates at 532.25-nm wavelength. The notation I_N designates the normalized intensity, in arbitrary units. (a) The pump wave is polarized on the slow axis. (b) The pump wave is polarized on the fast axis. (c), (d) The fiber is pumped at 15° of polarization with a total input power of 21 W. (e), (f) The fiber is pumped at 30° of polarization with a total input power of 19 W. (g), (h) The fiber is pumped at 45° of polarization with a total input power of 22 W.

ers exiting the fiber are monitored using a high speed photodiode FND 100 from EGG and a digital oscilloscope. The photodiode has been calibrated thanks to a power meter Scientech 372 and to a set of calibrated filters.

The signal is amplified in a photomultiplier Hamamatsu R 585, then sampled and averaged by a Boxcar SRS 250. The Boxcar is externally triggered by a signal coming from a photodiode which receives a reflection from the Nd:YAG pulse. The scanning of the spectrometer as well as the recording of the data are monitored by a PC.

B. Experimental study: Single-frequency-copropagation regime

In our first experimental study, the fiber is pumped by a Nd:YAG laser, operating around 532-nm wavelength. Figure 11 shows a typical example of the experimental observation of the effects of changing the polarization of the input wave on the MI phenomenon. The powers indicated in these figures, as also in all forthcoming figures, represent the input-wave peak powers. Furthermore, hereafter, the peaks that are present in all spectra are systematically normalized in such a way that the highest peak is always equal to 1 (in arbitrary units). Figures 11(a) and 11(b) show, respectively, the spectra obtained when the input wave is entirely polarized along a single birefringence axis. We observe, as expected, that no MI appears in both cases. The pump wave only generates several Raman peaks. Notice that in the experimental results that will be presented later on, the Raman effects will no longer be systematically shown in the figures whenever they will appear. The subsequent frames, Figs. 11(c) and 11(d), show that MI appears as soon as the input-wave power, $\approx$20 W, is distributed on the two birefringence axes. Figures 11(c) and 11(d), which correspond to the input wave polarized at 15° with respect to the slow axis, show two sidebands with relatively low amplitude. Figures 11(e) and 11(f), and 11(g) and 11(h), obtained, respectively, for a polarization of 30° and 45° with respect to the slow axis, show that the importance of the MI phenomenon increases as the polarization moves to 45°, that is, as the input powers on the two birefringence axes tend to become identical. This corresponds precisely to the behavior predicted by the ICE's (Fig. 2). Moreover we see in all spectra in Figs. 11(c)–11(h) that the OMF varies only very slightly as the polarization changes, as expected in the low-power region. On the other hand, Figs. 11(c)–11(h) clearly show a spectral broadening of the pump and the two sidebands due to self-phase modulation. We also see that the slow sideband grows much more quickly as the power increases than does the fast sideband. This well-known asymmetric behavior results from the effects of Raman gain and depletion for the Stokes and anti-Stokes bands, respectively [20,21].

In our second experimental study for the single-frequency-copropagation regime, the fiber is pumped by the Nd:YAG laser operating at 532-nm wavelength, with increasing input powers on the slow and fast axes. The spectra obtained are shown in Fig. 12. In Figs. 12(a) and 12(b) no MI is observed because the input powers are below the threshold powers required to compensate the fiber losses. In Figs. 12(c) and 12(d) the power levels increase and the MI gain becomes higher than the fiber losses and MI is thus observable. The subsequent frames show that as input powers increase, the sideband powers become increasingly large, and undergo Raman scattering, which explains the additional Raman peaks in the spectra. Those Raman peaks become slightly visible in Figs. 12(e) and 12(f), and are clearly visible in Figs. 12(g) and 12(h). Not all spectra obtained in this experimental study are shown in Fig. 12, but the main results are summarized in Table I. The two last data lines in this table ($P=17$ W) correspond to the case where the polarization moves towards the slow axis. We then observed, as predicted (see Fig. 2), that the OMF varies only slightly as one changes the polarization. In general, in Table I, the predicted values $F_{\text{mod-ICE}}$ and the observed values ($F_{\text{mod-expt}}$) agree within 9%, which corresponds to a quite satisfactory quantitative agreement.

C. Experimental study: Two-frequency-copropagation regime for small GVM

Observation of the critical gap

Figure 13 shows a sequence of experimental observations that exhibit the critical regime. For obtaining those spectra

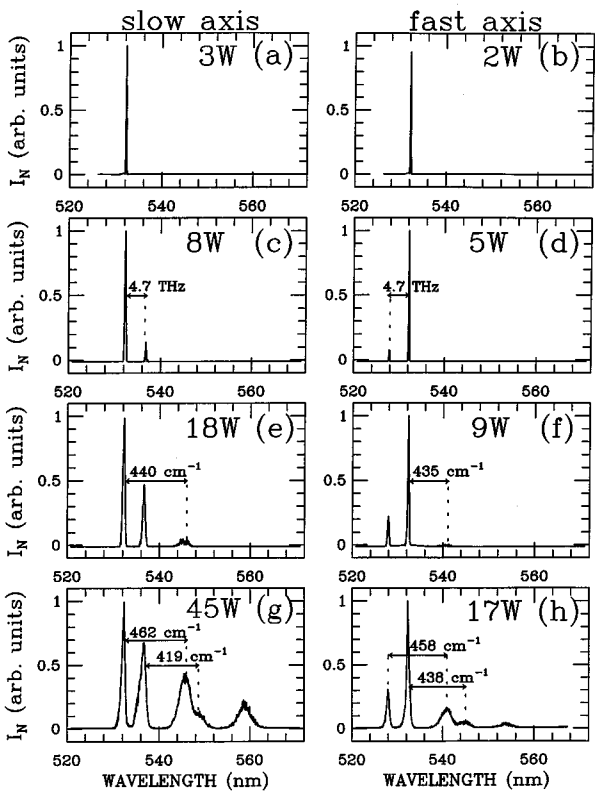

FIG. 12. Spectra of light emerging from the fiber for the single-frequency-copropagation regime, for increasing input powers P (on the fast axis) and Q (on the slow axis). The pump wave, operating at 532 nm, is polarized between the two birefringence axes. (a), (b) $Q=3$ W and $P=2$ W. (c), (d) $Q=8$ W and $P=5$ W. (e), (f) $Q=18$ W and $P=9$ W. (g), (h) $Q=45$ W and $P=17$ W.

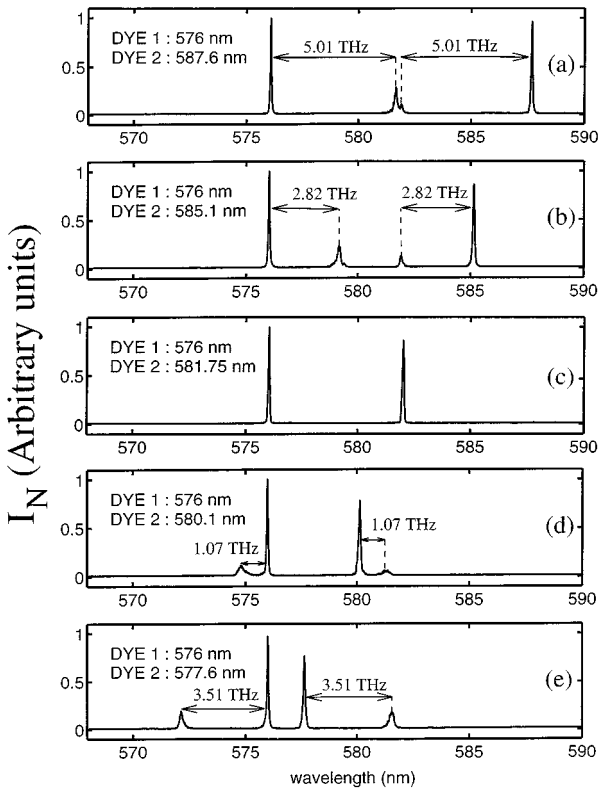

FIG. 13. Spectra of light emerging from the fiber for a two-frequency-copropagation regime for small positive and negative GVM, for decreasing wavelength separation between the pump waves. The fiber is pumped by two dye lasers, denoted ''DYE1'' and ''DYE2'' in the figures, polarized, respectively, along the fast and the slow axis. The spectra include the light coming from the two birefringence axes. (a) $\lambda_q=587.6$ nm. (b) $\lambda_q=585.1$ nm. (c) $\lambda_q=581.75$ nm. (d) $\lambda_q=580.1$ nm. (e) $\lambda_q=577.6$ nm.

we modified slightly the experimental apparatus shown in Fig. 10, in the following way: first, the Glan-Foucault analyzer was taken out of the apparatus in order to include in each spectrum the light emerging from the two birefringence axes. Second, the Nd:YAG laser operating at 532-nm wavelength was used to pump a second dye beam with a variable wavelength. So we used two waves produced, respectively, by a dye laser with a fixed wavelength $\lambda_{dye1}=576$ nm, and another dye laser with a variable wavelength λ_{dye2} in the range 577.6 nm$\leqslant\lambda_{dye2}\leqslant$587.6 nm. The wave λ_{dye1} was polarized along the fast axis, and therefore this wave corresponds to the wave that we called λ_p in the theoretical study.

TABLE I. Optimum modulation frequencies for the single-frequency-copropagation regime considered in Fig. 12. The observed values ($F_{\text{mod-expt}}$) and the predicted values ($F_{\text{mod-ICE}}$, $\Omega_{\text{opt-nl}}/2\pi$) are given for comparison.

		OMF (THz)		
$\lambda_p=\lambda_q=532$ nm		$F_{\text{mod-expt}}$	$F_{\text{mod-ICE}}$	$\frac{\Omega_{\text{opt-nl}}}{2\pi}$
$Q=8$ W	$P=5$ W	4.777	4.553	4.554
$Q=18$ W	$P=9$ W	4.715	4.498	4.499
$Q=22$ W	$P=11$ W	4.702	4.484	4.475
$Q=45$ W	$P=17$ W	4.722	4.374	4.357
$Q=66$ W	$P=17$ W	4.734	4.292	4.266

The wave λ_{dye2}, polarized along the slow axis, corresponds to λ_q. Figures 13(a)–13(e) were obtained, respectively, for different values of λ_{dye2} and by introducing the same input-wave power, $P=9$ W, in each birefringence axis. So each parameter set ($\lambda_{dye1}=576$ nm, λ_{dye2}, $P=9$ W) corresponds to an operating condition for the two-frequency copropagation described theoretically in Sec. II. The operating conditions were chosen by making use of the results in Fig. 7(b), where the small crosses labeled $[a]$, $[b]$, and so on, up to $[e]$ represent, respectively, the operating conditions used in Fig. 13; for example, the cross labeled $[a]$ represents the operating condition that we have used for obtaining the spectrum in Fig. 13(a), and so on.

Figure 13(a) shows that the wavelength $\lambda_{dye2}=587.6$ nm gives us, as expected, a MI phemenon, but where the two sidebands appear essentially at the same place in the spectrum, that is, almost midway between the two pump waves. As λ_{dye2} decreases, the OMF decreases and the sidebands go closer to the pump waves while their power decreases continuously [Fig. 13(b)]. The sideband powers decrease as the system approaches the critical regime. We observe indeed that when the wavelength difference is reduced to $\lambda_{dye2}-\lambda_{dye1}=581.75-576=5.75$ nm the power of the sidebands becomes zero [Fig. 13(c)]. We reemphasize that the corresponding parameter set ($\lambda_{dye1}=576$ nm, $\lambda_{dye2}=581.75$ nm, $P=9$ W) represents an operating condition within the

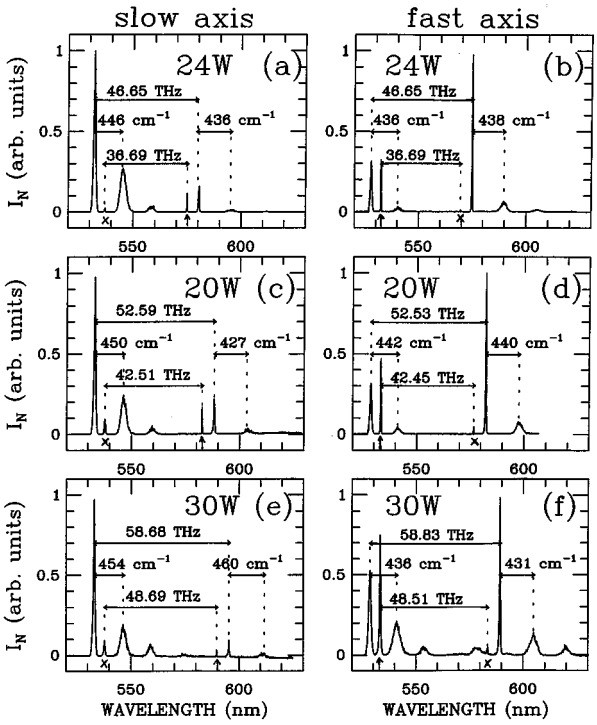

FIG. 14. Spectra of light emerging from the fiber for a two-frequency-copropagation regime with large GVM, for increasing wavelength separation between the pump waves. The fiber is pumped by a Nd:YAG laser operating at $\lambda_q = 532$-nm wavelength, polarized along the slow axis, and a dye laser of variable wavelength λ_p, polarized along the fast axis. In these experiments, the same input power P is introduced in the two birefringence axes. (a), (b) $\lambda_p = 575$ nm, $P = 24$ W. (c), (d) $\lambda_p = 581$ nm, $P = 20$ W. (e), (f) $\lambda_p = 588$ nm, $P = 30$ W.

critical gap predicted from the ICE's in Fig. 7(b), where MI disappears. Figure 13(c) therefore provides clear experimental evidence of the critical regime predicted in our theoretical investigations. Moreover we see in the subsequent frames, Figs. 13(d) and 13(e), that on decreasing further the wavelength separation, the MI regime reappears. Figures 13(d) and 13(e) show that the power of the sidebands begins again to increase as one moves away from the critical regime. The reappearance of MI therefore gives us the experimental evidence that for a given power P there exists a critical gap corresponding to a finite range of the wavelength separations between the pump waves.

Another important point to note is that the experimental observations in Figs. 13(a)–13(e), which correspond, respectively, to $\delta = -1.8630$, -1.0730, 0, 0.5411, and 1.3658 ps/m, show (as predicted) that the sidebands take place inside the frequency interval between the pump waves when $\delta < 0$, and outside of this interval for $\delta > 0$. Furthermore, the ICE prediction and the phase-matching formulas are satisfactorily verified, as shown in Fig. 9, where the diamonds represent the OMF for the experimental situations considered in Fig. 13.

D. Experimental study: Two-frequency-copropagation regime for large GVM

Figure 14 shows several experimental observations that we have made in the two-frequency-propagation regime by choosing the pump wavelengths in such a way as to obtain large GVM. The pump waves were produced, respectively, by a Nd:YAG laser at a fixed wavelength $\lambda_q = 532$ nm, polarized along the slow axis, and a dye amplified beam with a variable wavelength λ_p, according to the experimental setup in Fig. 10. Figures 14(a) and 14(b), 14(c) and 14(d), and 14(e) and 14(f) were obtained, respectively, for ($\lambda_p = 575$ nm, $P = Q = 24$ W), ($\lambda_p = 581$ nm, $P = Q = 20$ W) and ($\lambda_p = 588$ nm, $P = Q = 30$ W), which correspond, respectively, to $\delta = 18.4420$, 20.4300, and 22.6640 ps/m. The same power $P = Q$ was introduced on each birefringence axis in order that the importance of the MI phenomenon is maximum. In our experiments the two orthogonal linear polarizations at the fiber input were not perfectly controlled and a small amount of the power launched along the fast (slow) axis was always present along the slow (fast) axis. At large pump powers these residual powers can become sufficiently large to have visible effects on the observed spectra which are thus more complex. However, the corresponding additional peaks can be easily interpreted since they simply correspond to a situation which is symmetric with respect to the main pump waves. That is, when the residue of the pump ω_p is launched on the slow axis, and the residue of the pump ω_q along the fast axis, this situation leads to two additional sidebands whose frequencies can be obtained by just inverting δ in the theoretical description for large pump waves. In Fig. 14 the residues are indicated by small up arrows. We see in Fig. 14 that once created, the residues become new pump waves, and they contribute to developing two additional sidebands whose OMF differs clearly from the OMF for the pump-wave beams. The additional sidebands are indicated in Figs. 14(a)–14(f) by small crosses [note that the additional sideband is not clearly visible in Fig. 14(b)].

TABLE II. Optimum modulation frequencies for the two-frequency-copropagation regime considered in Fig. 14. The observed values ($F_{\text{mod-expt}}$) and the predicted values ($F_{\text{mod-ICE}}, \Omega_{\text{opt-nl}}/2\pi$) are given for comparison.

	OMF (THz)		
$\lambda_q = 532$ nm	$F_{\text{mod-expt}}$	$F_{\text{mod-ICE}}$	$\frac{\Omega_{\text{opt-nl}}}{2\pi}$
$\lambda_p = 575$ nm $P = 24$ W	46.6500	46.9896	46.9901
$\lambda_p = 581$ nm $P = 20$ W	52.5600	52.4112	52.4119
$\lambda_p = 588$ nm $P = 30$ W	58.7550	58.5902	58.5938

Table II summarizes all results of Fig. 14, and gives in addition the OMF obtained via the theoretical approaches considered previously. In that table, $F_{\text{mod-expt}}$ represents the experimental determination of the OMF for the two large pump-wave beams, averaged over the individual values for each birefringence axis. We observe an excellent agreement (within 0.8%) between the theoretical predictions and the experiments. On the other hand, we note in Fig. 14 the presence of several Raman peaks that are generated not only by the main pump beams, but also by the largest sidebands of those pump waves.

E. Experimental study showing some effects of the coherent coupling terms

To conclude this section on experimental results, we analyze in this subsection the condition of validity of the ICE

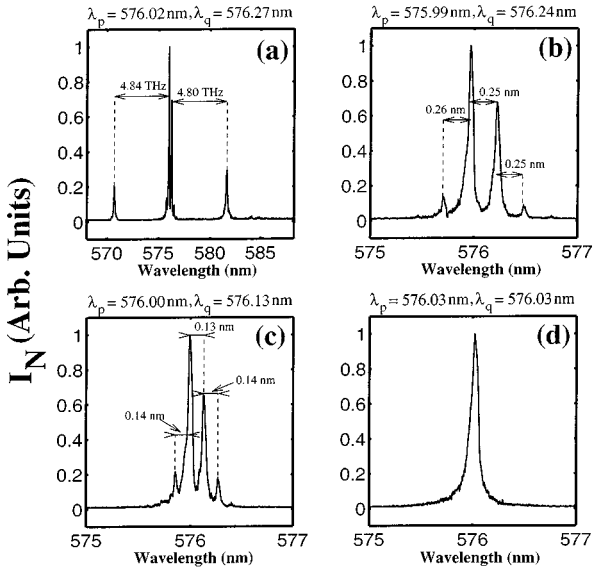

FIG. 15. Spectra of light showing the effects of the coherent coupling terms [in the right-hand side of the NLSE (4), (5)], for $P=Q=9$ W and different wavelength separations between the pump waves. The fiber is pumped by a Nd:YAG laser operating around $\lambda_p=576$-nm wavelength, polarized along the fast axis, and a dye laser of variable wavelength λ_p, polarized along the slow axis. The spectra include the light coming from the two birefringence axes. (a) $\lambda_p=576.02$ nm, $\lambda_q=576.27$ nm. (b) $\lambda_p=575.99$ nm, $\lambda_q=576.24$ nm. (c) $\lambda_p=576.00$ nm, $\lambda_q=576.13$ nm. (d) $\lambda_p=576.03$ nm, $\lambda_q=576.03$ nm.

model used to predict the MI features in highly birefringent fibers, and in particular, the existence of a critical gap in the frequency dependence of MI. We have discussed in Sec. II the role of the coherent coupling terms neglected in the ICE's. We have shown that these terms play a role only in a very narrow parameter range close to the condition of equal pump wavelengths. More precisely, we have found out, in a first approximation, that the beat length between the birefringence axes becomes appreciable only when the wavelength separation between the pump waves is of the order of $0.2\pm\varepsilon$ nm, where $\varepsilon<0.25$ nm is closely related to the fiber length. We have checked this prediction by observing the behavior of the system as λ_q approaches λ_p. Figure 15 shows several spectra measured at the fiber output for small wavelength separations between the pump waves: $\Delta\lambda=\lambda_q-\lambda_p=0.25$ nm [Figs. 15(a) and 15(b)], $\Delta\lambda=0.13$ nm [Fig. 15(c)], and $\Delta\lambda=0$ [Fig. 15(d)].

We see in Figs. 15(a)–15(c) that two additional peaks [which are only slightly visible in Fig. 15(a)] appear besides the two pump peaks. The resulting four peaks are equally spaced by about $\Delta\lambda$. Note that the system always generates MI sidebands but which take place well apart from the group of four peaks. These MI sidebands are shown only in Fig. 15(a) for the sake of clarity for the other spectra in Figs. 15(b)–15(d). The observed OMF, Fig. 15(a), averaged over the two birefringence axes and represented by the diamond symbol at $\lambda_q=576.27$ nm in Fig. 9, does not differ significantly from the value predicted by the ICE's.

The appearance of additional peaks besides the two pump waves in Figs. 15(a)–15(c) can be easily interpreted as being due to the coherent coupling terms in Eqs. (4) and (5). Indeed, from these equations, we see that the coherent coupling term in the equation of wave ω_p acts as a source term at the frequency $\omega_p-2|\Delta\omega|$, $\Delta\omega=\omega_q-\omega_p$, while the coherent coupling term in the equation of wave ω_q acts as a source term at the frequency $\omega_q+2|\Delta\omega|$. This means that the additional peaks due to these coupling terms will give to the spectrum the shape of four equally spaced peaks with frequency separation $|\Delta\omega|$ exactly as observed in Figs. 15(a)–15(c).

Figures 15(b) and 15(c) show that in decreasing the wavelength separation between the pump waves the additional peaks come closer to the pump peaks, and then quickly disappear as shown in Fig. 15(d), where $\Delta\lambda=0$ (single-frequency regime). On the other hand, when one increases $\Delta\lambda$ from the region of large beat length, the separation between the four peaks increases while the intensity of the additional peaks decreases down to zero. These results confirm the validity of our theoretical analysis of the role of the coherent coupling terms. They clearly show that these terms affect the system's dynamics only on a very small parameter range which is very far away from the condition of observation of the critical gap described above. In other words, the ICE model and its predictions are valid in the experimental condition of interest in the present paper.

IV. CONCLUSION

In the present paper we have set up a general picture of MI for the single-frequency-copropagation regime as well as for the two-frequency-copropagation regime. We have obtained experimental observations showing a richer spectrum of behavior for the two-frequency copropagation than for the single-frequency copropagation. That is, we have shown that qualitatively different behaviors manifest themselves depending on the wave-length separation between the pump waves. The greatest qualitative difference revealed by our theoretical investigations and experimentally verified is the existence of a nonlinearly induced gap in the frequency dependence of MI, namely, the existence of a range of wavelength separation for which MI disappears because of the reduction to zero of the GVM which has been made possible by the use of two wavelengths. This original result constitutes the main contribution of our report.

We can summarize our results as follows: with respect to previous work on the subject, we have completed the theoretical description of the system by including the analysis of the eigenvectors associated with the unstable eigenvalues representing MI. This analysis reveals that MI in the highly birefringent fiber generates only one sideband on each birefringence axis provided that the power is sufficiently lower than the critical power. However, as the power approaches the critical power the relative weights of the two other sidebands increase and become equal to those of the initially prominent sidebands. As regards the original part of the theoretical description we have shown by means of a simple analysis of the underlying FWM phase-matching conditions that the appearance of the critical regime can be interpreted as being due to the formation of a nonlinearly induced gap in the frequency dependence of MI. This analysis provides a deeper physical insight into the dynamics of MI in highly birefringent fibers and shows that the experimentally studied

critical regime results from strongly nonlinear dependence of the MI process. This nonlinear dependence allows us to use the terminology of modulational instability instead of simply four-wave mixing for what we have observed. This comment is related to the confusion which is common in the literature about the distinction between MI and FWM [28]. Both phenomena are of course intimately related and the distinction between them is more relevant to a problem of terminology than to the basic physical processes which originate them. Let us briefly discuss this issue: the possibility of obtaining phase-matched FWM by using different fiber modes is a well-known process, and using two different polarization modes of a single-mode fiber is just an example of strategy for obtaining phase matching. In fact, the experiments of FWM based on this principle were done already more than 20 years ago using multimode fibers [29] and were referred to as stimulated FWM. In this case phase matching is obtained by simply matching the propagation constants of the two fiber modes which enter into play. This phase-matching process uses the linear features of the multimode fiber and certainly does not require nonlinear dependence of the wave vectors. The situation is similar in the highly birefringent fiber where phase matching is obtained via the difference in the propagation constants associated with the fast and the slow axis. So one may object that what is observed in the highly birefringent fiber should be more rigorously referred to as FWM and not MI. The simplest example of MI is the one affecting a simple wave propagating in a fiber in the anomalous dispersion regime. In that case there is no other way to get phase matching of the FWM process than using the Kerr nonlinearity. In other words, the power dependence of the wave vectors is essential in the phase-matching process. This makes a fundamental distinction between MI and stimulated FWM.

Apart from the analysis of Ref. [30] where a slight nonlinear dependence of the sideband frequencies was observed, in most previous experimental works on FWM processes in highly birefringent fibers, power dependent phase-matching effects were not evidenced [20,21]. The main reason for this is that the critical power is well beyond any practical power levels in the single-frequency-copropagation regime. This means that the operating condition is always in the low-power limit of the theory for which phase-matched FWM is obtained with the condition $\Omega = \delta_0/\beta_2$ which only implies the linear characteristics of the fiber. Quite to the contrary, in our experiments, since we can approach the critical power by decreasing δ, we observe a strong nonlinear dependence of the phase-matching conditions. The most striking manifestation of the nonlinear dependence is the appearance of the nonlinearly induced gap in the frequency dependence of MI. In view of this experimentally evidenced nonlinear dependence of the phase-matching conditions, we believe that the use of the term modulational instability instead of simply stimulated FWM is fully justified.

Our experimental results can be summarized as follows: In the single-frequency-copropagation regime, FWM spectra have been observed and were found to be in good agreement with the theoretical prediction in the low-power limit, in a way very similar to what was already reported in Refs. [20,21] . In the two-frequency regime we have shown that, at large GVM, the general behavior is very similar to that observed in the single-frequency regime, namely, the wave dynamics can be easily explained in terms of classical FWM with no power dependence of phase-matching conditions. However, at small GVM, we have demonstrated the existence of a gap in the MI frequency dependence. This gap can only be explained via the power dependence of the phase-matching conditions. Its experimental evidence represents therefore a significant progress in the knowledge and understanding of the nonlinear dynamics of wave propagation in birefringent fibers.

Finally we have checked the validity of the ICE model by showing that the coherent coupling terms enter into play in a very restricted range of parameter located far from the parameter range of interest for the demonstration of the phase-matching power dependence. This result shows that the ICE constitutes an excellent model for the description of nonlinear wave propagation in highly birefringent fibers.

ACKNOWLEDGMENTS

This work was partly supported by the GDR POAN Science program. The Centre National de la Recherche Scientifique, The Ministère de l'Education Nationale, and the Conseil Régional de Bourgogne are also gratefully acknowledged for their financial support of this work. The work of M.H. has been partially supported by the FNRS and the PAI program of the Belgian Government. The authors would like to thank S. Wabnitz for helpful discussions.

[1] A. Hasegawa and W. F. Brinkman, IEEE J. Quantum Electron. **16**, 694 (1980).
[2] L. A. Ostrovskii, Zh. Tekh. Fiz. **33**, 905 (1963) [Sov. Phys. Tech. Phys. **8**, 679 (1964)].
[3] V. I. Bespalov and V. I. Talanov, Pis'ma Zh. Eksp. Teor. Fiz. **3**, 471 (1966) [JETP Lett. **3**, 307 (1966)].
[4] V. I. Karpman, Pis'ma Zh. Eksp. Teor. Fiz. **6**, 829 (1967) [JETP Lett. **6**, 277 (1967)].
[5] K. Tai, A. Hasegawa, and A. Tomita, Phys. Rev. Lett. **56**, 135 (1986).
[6] A. S. Gouveia-Neto, M. E. Faldon, A. S. B. Sombra, P. G. J. Wigley, and J. R. Taylor, Opt. Lett. **13**, 901 (1988).
[7] M. Nakasawa, K. Susuki, H. Kubota, and H. A. Haus, Phys. Rev. A **39**, 5768 (1989).
[8] M. Nakasawa, K. Susuki, H. Kubota, and H. A. Haus, IEEE J. Quantum Electron **25**, 2045 (1989).
[9] E. J. Greer, D. M. Patrick, P. G. J. Wigley, and J. R. Taylor, Opt. Lett. **15**, 851 (1990).
[10] Ting-Kuang Chiang, Nobuyuki Kagi, Thomas K. Fong, and Michel E. Marhic, IEEE Photonics Technol. Lett. **6**, 1041 (1994).
[11] K. Stenersen and R. K. Jain, Opt. Commun. **51**, 121 (1984).
[12] R. K. Jain and K. Stenersen, Appl. Phys. B **35**, 49 (1984).
[13] C. R. Menyuk, IEEE J. Quantum Electron **23**, 174 (1987).

[14] T. A. B. Kennedy and S. Wabnitz, Phys. Rev. A **38**, 563 (1988).
[15] S. Wabnitz, Phys. Rev. A **38**, 2018 (1988).
[16] E. A. Golovchenko and A. N. Pilipetskii, Sov. Lightwave Commun. **1**, 271 (1991).
[17] M. Haelterman, Opt. Commun. **111**, 86 (1994).
[18] C. De Angelis, M. Santagiustina, and S. Trillo, Opt. Lett. **19**, 335 (1994).
[19] C. De Angelis, M. Santagiustina, and S. Trillo, Phys. Rev. A **51**, 774 (1995).
[20] J. E. Rothenberg, Phys. Rev. A **42**, 682 (1990).
[21] P. D. Drummond, T. A. B. Kennedy, J. M. Dudley, R. Leonhardt, and J. D. Harvey, Opt. Commun. **78**, 137 (1990).
[22] S. G. Murdoch, R. Leonhardt, and J. D. Harvey, Opt. Lett. **20**, 866 (1995).
[23] Shiva. Kumar, A. Selvarajan, and G. V. Anand, J. Opt. Soc. Am. B **11**, 810 (1994).
[24] P. Tchofo Dinda, M. Haelterman, and G. Millot (unpublished).
[25] C. Roche, G. Millot, R. Chaux, and R. Saint-Loup, J. Chem. Phys. **101**, 2863 (1994).
[26] G. Fanjoux, G. Millot, R. Saint-Loup, R. Chaux, and L. Rosenmann, J. Chem. Phys. **101**, 1061 (1994).
[27] R. Chaux, C. Milan, G. Millot, B. Lavorel, R. Saint-Loup, and J. Moret-Bailly, J. Opt. (Paris) **19**, 3 (1988).
[28] S. Wabnitz (private communication).
[29] R. H. Stolen, IEEE J. Quantum Electron. **11**, 100 (1975).
[30] H. G. Park, J. D. Park, and S. S. Lee, Appl. Opt. **26**, 2974 (1987).